Chinese Chemical Letters 34 (2023) 107601

Contents lists available at ScienceDirect

Chinese Chemical Letters

journal homepage: www.elsevier.com/locate/cclet

Facile synthesis of defect-rich Fe-N-C hybrid from fullerene/ferrotetraphenylporphyrin as efficient oxygen reduction electrocatalyst for Zn-air battery

Hai Wang[a], Liyun Cao[a,*], Yongqiang Feng[a,*], Junsheng Chen[a], Weihang Feng[a], Tianmi Luo[a], Yuzhu Hu[a], Chengke Yuan[a], Yajuan Zhao[a], Yong Zhao[c], Koji Kajiyoshi[b], Yijun Liu[c], Zhenjiang Li[d], Jianfeng Huang[a,*]

[a] School of Material Science and Engineering, International S&T Cooperation Foundation of Shaanxi Province, Shaanxi University of Science and Technology, Xi'an 710021, China
[b] Kochi University, Research Laboratory of Hydrothermal Chemistry, Kochi 780-8520, Japan
[c] Guangdong Mona Lisa Group Co., Ltd., Foshan 528211, China
[d] College of Materials Science and Engineering, Qingdao University of Science and Technology, Qingdao 266042, China

ARTICLE INFO

Article history:
Received 11 May 2022
Revised 25 May 2022
Accepted 8 June 2022
Available online 13 June 2022

Keywords:
Oxygen reduction reaction
Electrocatalyst
Fullerene
Defect
Zn-air battery

ABSTRACT

Exploring remarkable oxygen reduction reaction (ORR) electrocatalysts for regenerative fuel cells and metal-air batteries is highly essential. Herein, a novel non-noble metal-based heterogeneous electrocatalyst with rich defects were successfully synthesized by liquid-liquid interfacial precipitation (LLIP) of fullerene (C_{60}) and ferrotetraphenylporphyrin (FeTPP) followed by one step pyrolysis. The obtained product annealed at 700 °C (C_{60}/FeTPP-700), when employed as ORR electrocatalyst, revealed a positive half-wave potential ($E_{1/2}$) of 0.877 V *vs.* reversible hydrogen electrode (RHE), which was superior to that of the commercial 25% Pt/C. Delightfully, the assembled Zn-air battery (ZAB) using C_{60}/FeTPP-700 as an air-electrode catalyst exhibited a high power density of 153 mW/cm^2, specific capacity of 668 mAh/g and long-term cycling stability for more than 250 h. Experimental results proved that the excellent electrocatalytic ORR activity of C_{60}/FeTPP-700 would attribute to the synergistic effect between FeN_x sites, Fe_3C/Fe nanoparticles and the structure defects. This work provides a feasible and simple method to prepare non-noble metal-based ORR electrocatalysts for the application of energy storage and conversion.

To balance energy demand and environmental pollution phenomenon, the research and use of new energy has become the global spotlight [1–3]. Up to now, in order to produce highly efficient, clean and sustainable energy, the electrochemical energy storage and conversion technologies have been widely explored, such as fuel cells [4,5] and metal-air batteries [6–8]. Notably, Zn-air battery (ZAB) becomes a safe and promising battery system because of its low cost, abundance of Zn and mild reaction conditions. In addition, the theoretical specific energy density (1086 Wh/kg) of ZAB is 2.5 times higher than that of lithium-ion battery [9]. Unfortunately, the development of ZAB still is full of challenges, *e.g.*, the sluggish kinetics of cathodic oxygen reduction reaction (ORR) restricts the performance and further application of these devices [10,11]. Thus, it is very essential to synthesize highly active and durable electrocatalysts for speeding up the ORR kinetics process. Noble metal species, in especial Pt-based materials, have been used as the most effective electrocatalyst for ORR [12]. However, their prohibitive cost and sensitivity to poisoning impede their extensive applications in practical life. Hence, it is of practical importance to pursue non-noble metal-based electrocatalysts with high efficiency and low cost [13,14].

In the past several years, tremendous efforts have been devoted to developing non-noble mental-based electrocatalysts for ORR and Zn-air battery [15–17]. Particularly, M-N-C (M = transition metal) hybrid nanostructure generally were created by introducing non-noble metal species and nitrogen, which show superior ORR electrocatalytic activity [18,19], because N-doped carbon is more electronegative than carbon, redistributing the electrons of neighboring carbon and enhancing the adsorption and dissociation of oxygen molecules [20]. Metalloporphyrin, particularly ferrotetraphenylporphyrin (FeTPP) can directly be used as precursors of M-N-C structure because of their chemical structures [21–23]. Compared to

* Corresponding authors.
E-mail addresses: caoliyun@sust.edu.cn (L. Cao), fengyq@sust.edu.cn (Y. Feng), huangjf@sust.edu.cn (J. Huang).

https://doi.org/10.1016/j.cclet.2022.06.024
1001-8417/

other carbon materials, fullerene possess unique spherical molecular structure with all sp^2-hybridized carbon atoms and conjugated systems. Although C_{60} has been widely studied for biomedical and optoelectronic applications, few C_{60}-based functional ORR electrocatalyst has been reported [24]. Gao *et al*. synthesized a class of new metal-free C_{60}-SWCNT electrocatalyst that fullerene (C_{60}) was adsorbed onto single-walled carbon nanotubes (SWCNTs) as an electron-acceptor to induce intermolecular charge-transfer with the SWCNTs [25]. Combination of metalloporphyrin and fullerene *via* charge-transfer interactions seems ideal for a highly efficient conversion [26–28]. Notably, the research of defective carbon engineering has attracted wide attention, there are three universal kinds of defective carbon electrocatalysts, such as defective carbons modified by heteroatoms, creating the intrinsic defective carbons by physical or chemical way and inducing/coordinating defective carbons by atomic metal [29,30]. In addition, carbon materials with rich defects can accelerate the electron transfer and oxygen diffusion [31,32], and expose more active sites [33,34]. The defects not only improve surrounding electronic structure, but also trap metal atoms to from new coordination structures [35]. However, generation of defects still is an uncontrollable process in the carbon-based electrocatalysts [36] and the defect-related sites has yet not been fully made clear in the design of electrocatalysts.

In this study, we reported a defect-rich Fe-N-C hybrid system containing Fe_3C/Fe nanoparticles obtained by one-step pyrolysis of the fullerene/FeTPP self-assembly. The synthesized C_{60}/FeTPP-700 catalyst exhibited outstanding ORR activity in alkaline media with a high half-wave potential of 0.877 V *vs.* reversible hydrogen electrode (RHE) and robust stability than commercial 25% Pt/C. The ZAB assembled by C_{60}/FeTPP-700 catalyst as cathode output a power density of 153 mW/cm^2 and specific capacity of 668 mAh/g, comparable to the benchmark 25% Pt/C + IrO_2 based ZAB. Experimental results indicated that the favorable electrocatalytic ORR activity of C_{60}/FeTPP-700 would attribute to the synergistic effect between FeN_x sites, Fe_3C/Fe nanoparticles and the structure defects. The present work may provide a new platform for fullerene nanomaterial in application of energy storage and conversion.

The catalyst product was prepared through the self-assembly of C_{60} and FeTPP as the metal and nitrogen source using liquid-liquid interfacial precipitation (LLIP) method. It has been established that fullerene molecule could interact with metalloporphyrin *via* π-π interaction to form a sandwich structure [37,38], as illustrated in Scheme S1 (Supporting information). Composition analysis of the C_{60}/FeTPP (Figs. S1 and S2 in Supporting information) suggested that the metalloporphyrin was successfully synthesized. After pyrolysis under H_2/Ar atmosphere, the metal moieties coordinated with nitrogen atoms was reduced to M-N-C species. The morphology of the product was characterized by SEM and TEM measurement. As shown in Fig. 1a and Fig. S3 (Supporting information), C_{60}/FeTPP-700 possessed a metal-based core enwrapped by carbon layer, similar to C_{60}/FeTPP-600 and C_{60}/FeTPP-800 (Figs. S4 and S5 in Supporting information). The high-resolution transmission electron microscopy (HRTEM) image (Fig. 1b) of C_{60}/FeTPP-700 clearly disclosed a hybrid phase. The crystal lattice spacing of 0.203 nm was assigned to the (101) plane of $FeN_{0.095}$, and the fringe spacing of 0.212 nm could be ascribed to the (121) facet of Fe_3C moiety. Notably, crystal defects such as edges and amorphous domains can be observed in the region between the two phases as marked by yellow dashed lines. The corresponding selected area electron diffraction (SAED) pattern displayed the (101) facets of $FeN_{0.095}$ and (121) and (211) facets of Fe_3C, further confirming the co-existence of FeN_x and Fe_3C, as shown in Fig. 1c. High-angle annular dark field (HAADF) TEM image and the corresponding element mapping (Fig. 1d) disclosed that the nanoparticles of FeN_x and Fe_3C were dispersed on the surface of carbon matrix.

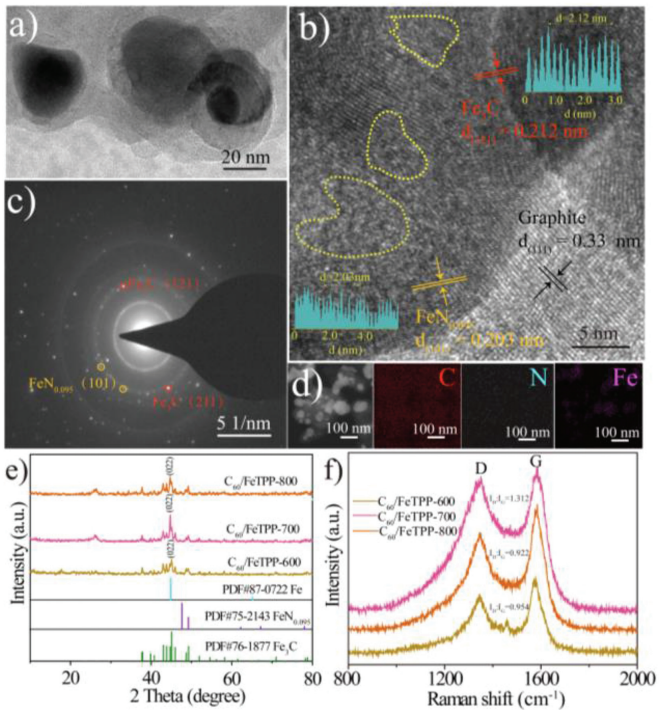

Fig. 1. Morphological characterization of the C_{60}/FeTPP-700. (a) TEM. (b) HRTEM. (c) SAED. (d) High-angle annular dark field (HAADF) TEM image and the element mapping of C, N, Fe. (e) XRD patterns and (f) Raman spectra for C_{60}/FeTPP-600, C_{60}/FeTPP-700 and C_{60}/FeTPP-800.

The phase composition of the samples was then determined by XRD. As shown in Fig. 1e and Fig. S6 (Supporting information), all three samples of C_{60}/FeTPP-T (T = 600, 700 and 800 °C) exhibited similar diffraction pattern, including the phase of FeN_x, Fe_3C and Fe with powder diffraction file (PDF) card number of 75-2143, 76-1877 and 87-0722, respectively. While the peak at around 26° for C_{60}/FeTPP-700 and C_{60}/FeTPP-800 were assigned to graphitic carbon, which was absent in the pattern of C_{60}/FeTPP-600 due to the lower annealing temperature, which was verified by the XRD result of the pure C_{60} annealed at 600 °C under the same conditions (Fig. S7 in Supporting information**)**. The characteristic (022) plane of Fe_3C (Fig. S8 in Supporting information) for C_{60}/FeTPP-700 was located at 44.76°, which was downshifted to 44.72° and 44.61° in the case of C_{60}/FeTPP-800 and C_{60}/FeTPP-600, respectively. Such lattice distortion would account for the defects observed in the TEM image. Notably, in the absence of C_{60}, the as-obtained FeTPP-700 exhibited a pure iron carbide without obvious defects (Figs. S9 and S10 in Supporting information), indicating that fullerene cage would facilitate the formation of structure defects. Besides, the Raman spectra display two broad peaks at around 1350 and 1578 cm^{-1} (Fig. 1f), corresponding to the D-band and G-band of amorphous carbon, respectively [39–41]. The results revealed that the integrated area ratio of D band to G band (I_D/I_G) value of C_{60}/FeTPP-700 (1.312) is higher than those of C_{60}/FeTPP-600 (0.954) and C_{60}/FeTPP-800 (0.922), suggesting a more disordered carbon structure of C_{60}/FeTPP-700. Generally, it is true that introducing Fe can enhance the graphitization degree at higher temperature [42], hence the increased proportion of defect in C_{60}/FeTPP-700, which has a positive effect on the electrocatalytic performance [43], indicating that the fullerene cage played a critical role in tuning the nanostructure of the catalyst. In order to further examine the porosities in each catalyst, N_2 adsorption/desorption isotherms were recorded, from which BET surface areas and pore size distribution curves were calculated. As

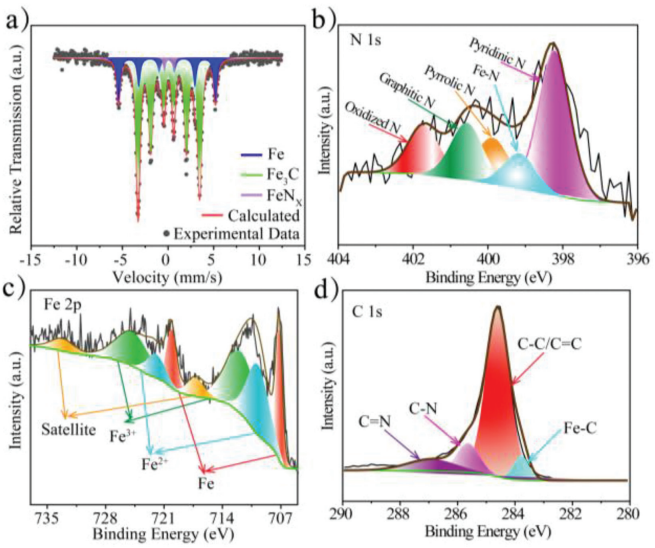

Fig. 2. (a) ^{57}Fe Mössbauer spectroscopy of C_{60}/FeTPP-700. High-resolution XPS spectra of C_{60}/FeTPP-700 for (b) N 1s, (c) Fe 2p and (d) C 1s.

shown in Fig. S11 (Supporting information), all catalysts exhibited a type-IV isotherm with a similar mesoporous structure. The specific surface area was determined to be 62.8, 60.5 and 59.9 m^2/g for C_{60}/FeTPP-600, C_{60}/FeTPP-700 and C_{60}/FeTPP-800, respectively. And the pore size of these catalysts distributed around 3.8 nm. The porous architecture of C_{60}/FeTPP-700 was supposed to facilitate the mass transport and promote the utilization of active site during ORR [16,44].

The Mössbauer spectra is a powerful tool to probe the intrinsic electronic structure [45]. In order to acquire the detail information about Fe species, the C_{60}/FeTPP-700 catalyst was further investigated with ^{57}Fe Mössbauer spectroscopy at room temperature. As shown in Fig. 2a, it is notable that the curve of C_{60}/FeTPP-700 could be well fitted into one doublet (D) and two sextets (Sextet 1 and Sextet 2), corresponding to FeN_x, Fe and Fe_3C, respectively [46–48]. The fitting parameters are summarized in Table S1 (Supporting information). The typical isomer shift (IS) values of 0.12, −0.12 and 0.07 mm/s were ascribed to FeN_x, Fe, Fe_3C, respectively, matching well with the component of C_{60}/FeTPP-700 observed in the XRD and TEM results. To obtain more information about elemental composition and chemical states, the samples were subjected to XPS analysis. XPS survey spectra (Fig. S12 in Supporting information) showed obvious C 1s, N 1s, O 1s and Fe 2p signals for C_{60}/FeTPP-T, and no binding energy signals for other elements were detected. The N 1s spectrum of C_{60}/FeTPP-700 (Fig. 2b) could be deconvoluted into five peaks marked as pyridinic N (398.2 eV), Fe-N (399.1 eV), pyrrolic N (399.8 eV), graphitic N (400.5 eV) and oxidized N (401.7 eV), respectively [49]. Due to the electron-donating properties, the rational arranged pyridinic N can serve as metal-coordination sites, and enable to capture proton and O_2 molecule during the electrocatalytic ORR process [50]. Therefore, the high contents of pyridinic N in C_{60}/FeTPP-700 (Fig. S13 and Table S2 in Supporting information) might facilitate the ORR activity. In Fig. 2c, the high-resolution Fe 2p spectrum of C_{60}/FeTPP-700 was split into three couple peaks with a pair of satellite peaks, where the peaks centered at 710.0 and 723.0 eV were respectively assigned to $2p_{3/2}$ and $2p_{1/2}$ of Fe^{2+} corresponding to Fe-N bonding in $FeN_{0.095}$, and the peaks at around 717.6 and 733.2 eV were belonged to satellite [51]. The peaks located at 711.9 and 726.6 eV were ascribed to $2p_{3/2}$ and $2p_{1/2}$ of Fe^{3+}corresponding to Fe-C bonding in Fe_3C [52], and the signal at around 707.4 and 720.3 eV can be attributed to zero-valence Fe [53]. These results are consistent with Mössbauer spectroscopy, the formation of Fe^{2+} and Fe^{3+} may be caused by electron transfer and Fe tendency to lose extranuclear electrons. N has strong coordination ability and is easy to form Fe-N. The C 1s spectrum of C_{60}/FeTPP-700, as shown in Fig. 2d, could be deconvoluted into four peaks, which can be assigned to Fe-C (283.8 eV), C-C/C=C (284.6 eV), C-N (285.6 eV) and C=N (286.9 eV), respectively [18,41,54].

The ORR catalytic performance of C_{60}/FeTPP-700 was conducted in O_2-saturated 0.1 mol/L KOH using a standard three-electrode system equipped on a Pine instrument. Before test, the reference electrode was experimentally calibrated against RHE by CV scanning in the voltage of ORR in H_2-saturated 0.1 mol/L KOH with the scan rate of 10 mV/s (Fig. S14 in Supporting information). For comparison, C_{60}/FeTPP-600, C_{60}/FeTPP-800 and the commercial 25% Pt/C were also examined. Fig. S15 (Supporting information) displayed the CV curves of C_{60}/FeTPP-700, which showed obvious reduction peak in O_2-saturated 0.1 mol/L KOH solution, whereas no peak could be observed within the same potential region in the N_2-saturated solution, suggesting an effective ORR process on C_{60}/FeTPP-700 in alkaline media. The ORR activities of samples were further investigated by LSV polarization curves (Fig. 3a). It can be seen that C_{60}/FeTPP-700 exhibited a superior ORR activity with higher half-wave potential ($E_{1/2}$, 0.877 V *vs.* RHE) toward C_{60}/FeTPP-600 (0.797 V *vs.* RHE) and C_{60}/FeTPP-800 (0.827 V *vs.* RHE), even surpassed the commercial 25% Pt/C (0.852 V *vs.* RHE), and comparable to many recently-reported ORR electrocatalyst (Table S3 in Supporting information). The specific mass activity is displayed in Fig S16, specifically, the C_{60}/FeTPP-700 still exhibited superior ORR activity compared with 25% Pt/C. The reaction kinetics was then evaluated by the Tafel plot. As shown in Fig. 3b, the C_{60}/FeTPP-700 displayed the lower Tafel slop (74.84 mV/dec) compared with C_{60}/FeTPP-600 (92.45 mV/dec), C_{60}/FeTPP-800 (116.82 mV/dec) and the commercial 25% Pt/C (88.00 mV/dec). The kinetic current density (J_k) derived from the Tafel plot was compared as shown in Fig. 3c. The lowest Tafel slop and highest J_k demonstrated that C_{60}/FeTPP-700 possessed a much faster electrocatalytic reaction kinetics during the ORR process. To get insight to the active sites for ORR in C_{60}/FeTPP-700, supplementary experiments were performed by poisoning FeN_x sites with SCN^-. It has been reported that there is a strong interaction between SCN^- ion and FeN_x site [55]. We obtained the LSV curves of C_{60}/FeTPP-700 in O_2-saturated 0.1 mol/L KOH with 0.01 mol/L SCN^- as displayed in Fig. 3d (blue line). The result implied that the current density of C_{60}/FeTPP-700 reduced significantly poisoned by SCN^-. Subsequently, the another LSV curves of fresh C_{60}/FeTPP-700 after poisoning by 0.1 mol/L HCl in O_2-saturated 0.1 mol/L KOH was shown in Fig. 3d (magenta line), in which the current density negatively shifted compared with the value of the initial 0.1 mol/L KOH. Particularly, the shift of the LSV curve after poisoning by 0.1 mol/L HCl indicated that Fe_3C and Fe species in the hybrid C_{60}/FeTPP-700 catalyst would probably in part make a contribute to the ORR process. Moreover, when the fullerene was absent in C_{60}/FeTPP-700 (Fig. S17 in Supporting information), the ORR performance decreased remarkably, indicating that C_{60} molecules also played a critical role in improving the ORR activity by tuning the defect in C_{60}/FeTPP-700. Therefore, the superior ORR activity of C_{60}/FeTPP-700 should be attributed to the synergetic effect of Fe-N-C species, Fe_3C and Fe nanoparticles and the structure defects.

Furthermore, the kinetic electron transfer numbers (n) of C_{60}/FeTPP-700 were evaluated based on K-L equation at various rotating speeds (Fig. 3e). The parallel K-L plots displayed a fine linear relationship between j^{-1} and $\omega^{-1/2}$ in the range of 0.4 V to 0.7 V, implying a first-order reaction kinetics. The value of n was calculated to be 3.98-4.02, implying a nearly $4e^-$ transfer pathway and direct electrocatalytic reduction of O_2 to OH^- species. The ultralow hydrogen peroxide (H_2O_2) yield (less than

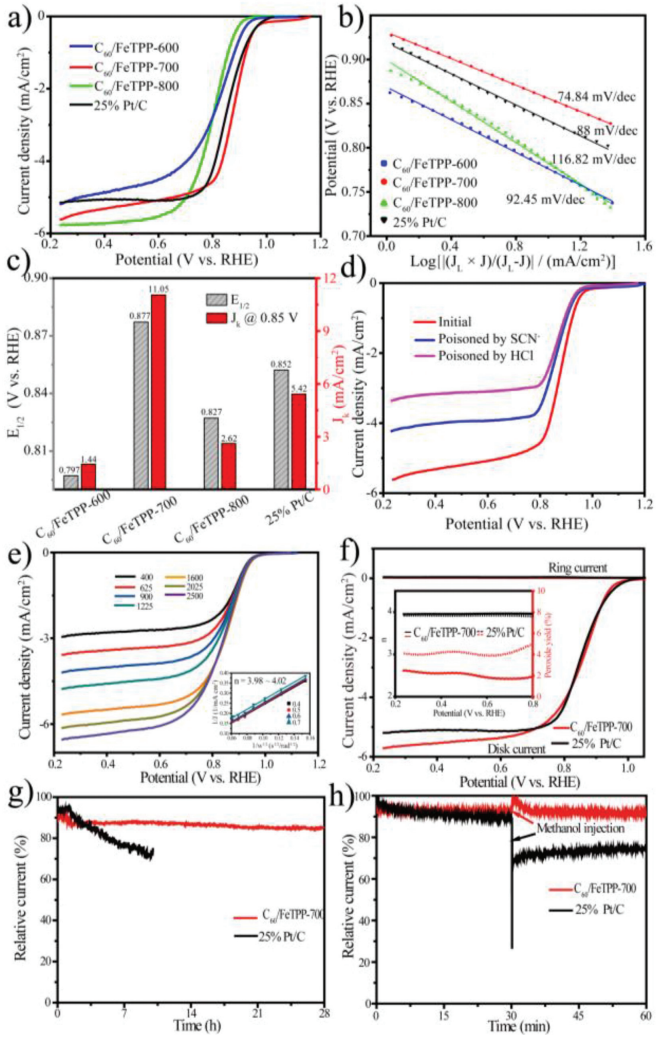

Fig. 3. Evaluation of electrocatalytic performance of C_{60}/FeTPP-700 for ORR. (a) ORR polarization curves of C_{60}/FeTPP-600, C_{60}/FeTPP-700, C_{60}/FeTPP-800 and 25% Pt/C catalysts tested in O_2-saturated 0.1 mol/L KOH solution at the rotation speed of 1600 rpm with a scan rate of 10 mV/s. (b) The corresponding Tafel plots derived from (a). (c) Comparison of $E_{1/2}$ and J_k at 0.85 V for various prepared catalysts. (d) Steady-state ORR polarization curves of C_{60}/FeTPP-700 tested in O_2-saturated 0.1 mol/L KOH with (blue line) poisoning by 0.01 mol/L SCN^-, and one recorded after poisoning by 0.1 mol/L HCl in O_2-saturated 0.1 mol/L KOH (magenta line). ORR activity measurement of C_{60}/FeTPP-700. (e) LSV curves of C_{60}/FeTPP-700 at various rotation rates (inset showing K-L plots). (f) LSV curves of C_{60}/FeTPP-700 and 25% Pt/C on RRDE in O_2-saturated 0.1 mol/L KOH at the rotation speed of 1600 rpm, inset showing the electron transfer number (n) and peroxide yields based on RRDE tests for C_{60}/FeTPP-700. (g) The chronoamperometric response of C_{60}/FeTPP-700 and 25% Pt/C at 0.6 V. (h) methanol crossover effect of C_{60}/FeTPP-700 and 25% Pt/C at 0.6 V in O_2-saturated 0.1 mol/L KOH electrolyte with injection of 10 mmol/L methanol at around 30 min.

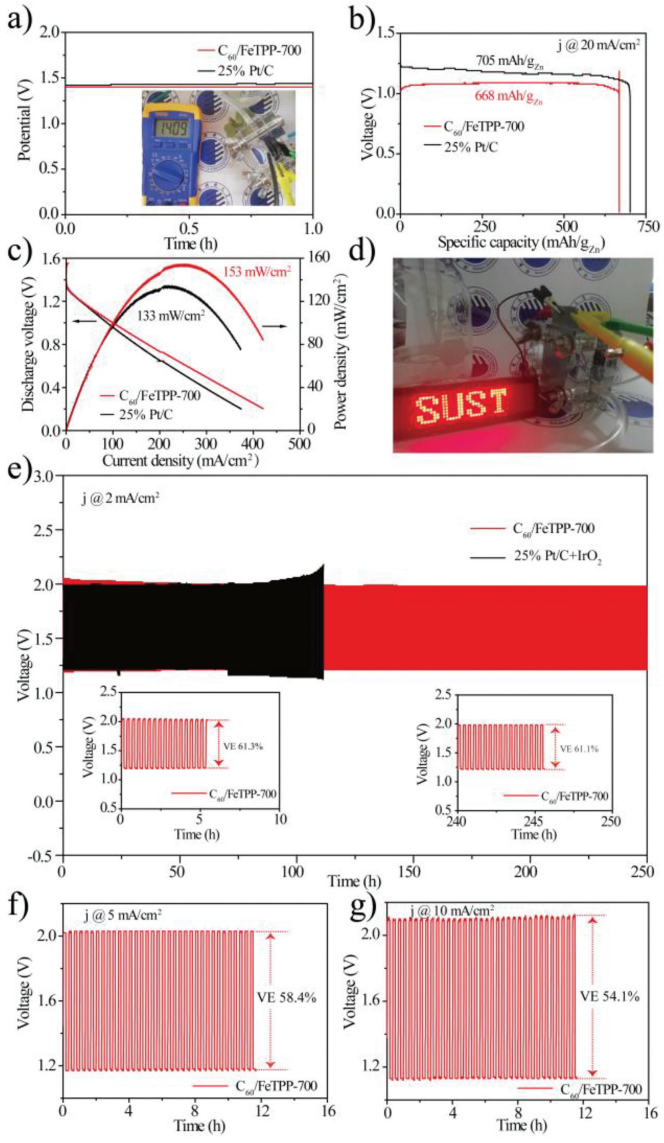

Fig. 4. ZAB battery performance test. (a) Open circuit potential (OCP) plot of the ZAB with C_{60}/FeTPP-700 and precious mental catalyst for 1 h in 6.0 mol/L KOH electrolytes, respectively. The inset photograph shows the OCP measured by multimeter. (b) The specific capacity plots at 20 mA/cm^2 and (c) discharge polarization and power density plots of the ZAB assembled by C_{60}/FeTPP-700 and precious mental catalyst. (d) Photograph of one C_{60}/FeTPP-700-based ZAB used to light LED that notes "SUST". Charge and discharge polarization curves of the ZABs at various current density, (e) 2 mA/cm^2; (f) 5 mA/cm^2; (g) 10 mA/cm^2.

3.0%) and the corresponding n value (about 4.0) obtained from the RRDE test (Fig. 3f) further confirmed a desirable 4e$^-$ ORR pathway for C_{60}/FeTPP-700, much favorable than the commercial 25% Pt/C. The long-term stability was then measured by chronoamperometric method. As shown in Fig. 3g, C_{60}/FeTPP-700 exhibited excellent durability with a high current retention at 0.6 V after 28 h in O_2-saturated 0.1 mol/L KOH, quite superior to the commercial 25% Pt/C. The long-term stability of C_{60}/FeTPP-700 was further evaluated by accelerated CV test. The LSV curve is almost unchanged after 1000 cycles (Fig. S18 in Supporting information). Furthermore, the high-resolution Fe 2p spectrum (Fig. S19 in Supporting information) and the TEM image (Fig. S20 in Supporting information) of C_{60}/FeTPP-700 indicated that the morphology and chemical state of was C_{60}/FeTPP-700 kept stable after the stability test. In addition, Fig. 3h showed that negligible current decay was observed for C_{60}/FeTPP-700 with the injection of methanol into electrolyte, while 25% Pt/C catalyst suffered from a quick drop, suggesting a glorious tolerance of C_{60}/FeTPP-700 to methanol.

Encouraged by its outstanding ORR performance of C_{60}/FeTPP-700, a primary Zn-air battery using C_{60}/FeTPP-700 as the cathodic electrode was assembled. Meanwhile, precious metal catalyst 25% Pt/C was chosen as a reference. As shown in Fig. 4a, the ZAB of C_{60}/FeTPP-700 possesses an open circuit potential (OCP) about 1.4 V comparable to that of precious 25% Pt/C catalyst-based battery. Further, Fig. 4b disclosed that the specific capacity of C_{60}/FeTPP-700 based ZAB was calculated to be 668 mAh/g based on the mass loss of Zn foil at a current density of 20 mA/cm^2, close to that of the battery assembled by 25% Pt/C catalyst (705 mAh/g). The power density was then obtained from the discharging polarization

curve as shown in Fig. 4c. the ZAB assembled using C_{60}/FeTPP-700 possessed a peak power density of 153 mW/cm^2 at 251 mA/cm^2, larger than that of the ZAB assembled using 25% Pt/C catalyst (133 mW/cm^2 at 220 mA/cm^2). The performance of the present ZAB based on C_{60}/FeTPP-700 was comparable with many other related ZAB batteries reported recently (Table S4 in Supporting information). In practice, as shown in Fig. 4d, one C_{60}/FeTPP-700-based ZAB enabled to light up a LED screen for more than 24 h at room temperature. Besides, inspired by the oxygen evolution property of C_{60}/FeTPP-700 (Fig. S21 in Supporting information), a rechargeable ZAB based on C_{60}/FeTPP-700 was fabricated. As showed in Fig. 4e, the ZAB of C_{60}/FeTPP-700 displayed a significant stable discharge and charge potential at 2 mA/cm^2 over 250 h without obvious potential decay and the round-trip efficiency kept stable from 61.3% to 61.1% during the whole charging-discharging process. On the contrary, the ZAB of 25% Pt/C + IrO_2 catalyst appeared a wide charge-discharge gap after 100 h. Further, the robust durability of the ZAB of C_{60}/FeTPP-700 was further evidenced by galvanostatic charge-discharge at 5 and 10 mA/cm^2, respectively (Figs. 4f and g). After 10 h, the ZAB of C_{60}/FeTPP-700 still maintains a high voltage efficiency of 58.4% (5 mA/cm^2) and 54.1% (10 mA/cm^2).

In summary, a defect-rich hybrid catalyst containing Fe-N-C species and Fe_3C/Fe nanoparticles imbedded on the carbon matrix was successfully prepared, which was derived from the pyrolysis of a fullerene/FeTPP assembly. The C_{60}/FeTPP-700 exhibited efficient ORR performance with higher half-wave potential (0.877 V *vs*. RHE) superior to commercial 25% Pt/C and robust catalytic durability. The Zn-air battery assembled by C_{60}/FeTPP-700 as cathode displayed a peak power density of 153 mW/cm^2 and specific capacity of 668 mAh/g, which was comparable to the ZAB fabricated by 25% Pt/C and IrO_2. Besides, the rechargeable ZAB possessed a long-term cycling stability (more than 250 h) and high round-trip efficiency (>61%). It was found that the synergistic effect between the FeN_x sites, Fe_3C/Fe nanoparticles and the structure defects in C_{60}/FeTPP-700 would account for the superior ORR performance. This work provided a simple and effective technique to synthesize N-coordination carbon-based non-noble metal electrocatalyst for energy storage and conversion.

Declaration of competing interest

The authors declare that they have no known competing financial interests or personal relationships that could have appeared to influence the work reported in this paper.

Acknowledgments

This work was supported by the National Natural Science Foundation of China (Nos. 52073166, 52072226), the Key Program for International S&T Cooperation Projects of Shaanxi Province (Nos. 2020KW-038, 2020GHJD-04), and Scientific Research Program Funded by Shaanxi Provincial Education Department (No. 20JY001), Science and Technology Resource Sharing Platform of Shaanxi Province (No. 2020PT-022). Dr. Y.Q. Feng was grateful for the support from the Science and Technology Youth Stars Project of Shaanxi Province (No. 2021KJXX-35).

Supplementary materials

Supplementary material associated with this article can be found, in the online version, at doi:10.1016/j.cclet.2022.06.024.

References

[1] M. Xiao, Z. Xing, Z. Jin, et al., Adv. Mater. 32 (2020) 2004900.
[2] R. Zhong, C. Zhi, Y. Wu, et al., Chin. Chem. Lett. 31 (2020) 1588–1592.
[3] D. He, L. Cao, J. Huang, et al., J. Energy Chem. 47 (2020) 263–271.
[4] J. Li, M.T. Sougrati, et al., Nat. Catal. 4 (2021) 10–19.
[5] P. Moni, M.G. Pollachini, M. Wilhelm, et al., ACS Appl. Energy Mater. 2 (2019) 6078–6086.
[6] R. Meng, C. Zhang, Z. Lu, et al., Adv. Energy Mater. 23 (2021) 2100683.
[7] X. Fu, G. Jiang, G. Wen, et al., Appl. Catal. B 293 (2021) 120176.
[8] Z. Zhu, Q. Xu, Z. Ni, ACS Sustainable Chem. Eng. 9 (2021) 13491–13500.
[9] D. Yang, L. Zhang, X. Yan, et al., Small Methods 1 (2017) 1700209.
[10] X. Hai, X. Zhao, N. Guo, et al., ACS Catal. 10 (2020) 5862–5870.
[11] M. Wang, K. Su, M. Zhang, et al., ACS Sustainable Chem. Eng. 9 (2021) 13324–13336.
[12] Q. Shu, Z. Xia, W. Wei, et al., ACS Appl. Energy Mater. 2 (2019) 5446–5455.
[13] H.-S. Oh, H. Kim, J. Power Sources 212 (2012) 220–225.
[14] L. Chen, X. Xu, W. Yang, et al., Chin. Chem. Lett. 31 (2020) 626–634.
[15] H. Peng, M. Zhang, K. Sun, et al., Appl. Surf. Sci. 529 (2020) 147174.
[16] X. Xie, L. Peng, H. Yang, et al., Adv. Mater. 23 (2021) 2101038.
[17] L. Li, J. Yang, H. Yang, et al., ACS Appl. Energy Mater. 1 (2018) 963–969.
[18] T. Jiang, W. Jiang, Y. Li, et al., Carbon 180 (2021) 92–100.
[19] M. Zhang, B. Yang, T. Yang, et al., Chin. Chem. Lett. 33 (2022) 362–367.
[20] H. Zhao, C. Sun, Z. Jin, et al., J. Mater. Chem. A 2 (2015) 11736.
[21] L. Xie, X.P. Zhang, et al., Angew. Chem. Int. Ed. 60 (2021) 7576–7581.
[22] Z. Liang, H. Guo, G. Zhou, et al., Angew. Chem. Int. Ed. 60 (2021) 8472–8476.
[23] Y. Feng, X. Wang, J. Huang, et al., Chem. Eng. J. 390 (2020) 124525.
[24] W. Xu, W. Huang, X. Lu, Mater. Today Nano (2020) 100081.
[25] R. Gao, Q. Dai, F. Du, et al., J. Am. Chem. Soc. 141 (2019) 11658–11666.
[26] T. Hasobe, A.S. Sandanayaka, T. Wada, et al., Chem. Commun. 29 (2008) 3372–3374.
[27] S. Zheng, J. Zhong, W. Matsuda, et al., Nano Res. 11 (2018) 1917–1927.
[28] M. Morisue, G. Saito, D. Sasada, et al., Langmuir 36 (2020) 13583–13590.
[29] Y. Jia, L. Zhang, A. Du, et al., Adv. Mater. 28 (2016) 9532–9538.
[30] X. Yan, Y. Jia, X. Yao, Chem. Soc. Rev. 47 (2018) 7628.
[31] L. Li, L. Zhang, Z. Xu, et al., Carbon 189 (2022) 634–641.
[32] J. Zhu, S. Mu, Adv. Funct. Mater. 30 (2020) 2001097.
[33] F. Dong, M. Wu, G. Zhang, et al., Chem. Asian J. 15 (2020) 3737–3751.
[34] Z. Xiao, C. Xie, Y. Wang, et al., J. Energy Chem. 53 (2021) 208–225.
[35] Y. Jia, K. Jiang, H. Wang, et al., Chem 5 (2019) 1371–1397.
[36] J. Zhang, Y. Sun, J. Zhu, et al., Nano Energy 52 (2018) 307–314.
[37] B. Wang, S. Zheng, A. Saha, et al., J. Am. Chem. Soc. 139 (2017) 10578–10584.
[38] F.S.T.D. Sun, C.A. Reed, L. Chaker, et al., J. Am. Chem. Soc. 124 (2002) 6604–6612.
[39] Y. Lin, K. Liu, K. Chen, et al., ACS Catal. 11 (2021) 6304–6315.
[40] P. Mallet-Ladeira, P. Puech, C. Toulouse, et al., Carbon 80 (2014) 629–639.
[41] P. Guo, L. Cao, R. Wang, et al., Adv. Funct. Mater. 30 (2020) 2000208.
[42] H. Li, Y. Wen, M. Jiang, et al., Adv. Funct. Mater. 31 (2021) 2011289.
[43] X. Cui, L. Gao, S. Lei, et al., Adv. Funct. Mater. 10 (2020) 2009197.
[44] W. Wang, J. Luo, W. Chen, et al., J. Mater. Chem. A 4 (2016) 12768–12773.
[45] Y. Feng, P. Dong, L. Cao, et al., J. Mater. Chem. A 9 (2021) 2135–2144.
[46] U.I. Kramm, L. Ni, S. Wagner, Adv. Mater. 31 (2019) 1805623.
[47] J. Hu, S. Wang, J. Yu, et al., Environ. Sci. Technol. 55 (2021) 1260–1269.
[48] K. Strickland, E. Miner, Q. Jia, U. Tylus, et al., Nat. Commun. 6 (2015) 7343.
[49] Y. Lei, F. Yang, H. Xie, et al., J. Mater. Chem. A 39 (2020) 20629–20636.
[50] Y. Zhao, K. Watanabe, K. Hashimoto, J. Am. Chem. Soc. 134 (2012) 19528–19531.
[51] W. Qiu, N. Yang, D. Luo, et al., Appl. Catal. B 293 (2021) 120216.
[52] Z. Wu, X. Xu, B. Hu, et al., Angew. Chem. Int. Ed. 54 (2015) 8179–8183.
[53] Y. Xing, Z. Yao, W. Li, et al., Angew. Chem. Int. Ed. 16 (2021) 8971–8977.
[54] Z. Yang, C. Zhao, Y. Qu, et al., Adv. Mater. 31 (2019) 1808043.
[55] L. Zhao, Y. Zhang, L. Huang, et al., Nat. Commun. 10 (2019) 1278.